SEDIMENTOLOGY the journal of the International Association of Sedimentologists

Sedimentology (2022) doi: 10.1111/sed.13046

Biomineralization of ordered dolomite and magnesian calcite by the green alga *Spirogyra*

PABLO DEL BUEY and M. ESTHER SANZ-MONTERO
Department of Mineralogy and Petrology, Complutense University of Madrid, 28040, Madrid, Spain (E-mail: mesanz@ucm.es)

Associate Editor – Mike Rogerson

ABSTRACT

The formation of ordered dolomite under Earth's surface conditions remains a challenge, although many researchers have now shown that microbes can facilitate the precipitation of this common mineral. This study provides the first evidence of dolomite biomineralization by the green alga *Spirogyra* (Zygnematales, Chlorophyta), a globally dispersed lacustrine genus. Microbial mats formed by *Spirogyra* occur in the hyperalkaline and ephemeral lake Caballo Alba, located in Central Spain and characterized by water solutions with high Mg/Ca ratios. Microscopic, geochemical, mineralogical and cytochemical studies have shown that accumulations of carbonates occur within different cells and locations of the alga. Biominerals mostly consist of single crystals of magnesian calcite and dolomite with variable proportions of Ca^{2+} and Mg^{2+}. High-resolution transmission electron microscopy and selected area electron diffraction patterns of the carbonates confirm the pervasive presence of super-lattice reflections typical of ordered dolomite in compositions with greater than 32 mol% $MgCO_3$. The curved surfaces of some carbonate crystals and their attachment to the organic surfaces represent imprints of a confined growth in compartments that act as a template for crystal nucleation and shape the crystals. Dyes reveal chemical differences in these compartments which explain the polymineral biomineralization and suggest that the alga do not strictly control the precipitation process. Zygnematales algae related with *Spirogyra* date back possibly to the Early Palaeozoic, thus suggesting that dolomite biomineralization could have been a common process through the Phanerozoic. This discovery provides new insight into the biotic formation of orderly dolomite and aids in the reconstructions of past lacustrine environments of dolomite deposition.

Keywords Biomineralization, green alga, highly alkaline lake, orderly dolomite, polymineral.

INTRODUCTION

Microbialites are carbonate organosedimentary structures that result from the mineralization of benthic microbial mats (Burne & Moore, 1987) and have a long geological record. While in recent decades much research has been carried out into mineralization of benthic microbial mats, mostly dominated by *Cyanobacteria* (Dupraz *et al.*, 2009, and references therein), few studies have been conducted into suspended microbial mats, which are also common in inland wetlands and can contribute to the formation of carbonates (Stevenson, 1996), influencing their environments. Free-floating mats, dislodged from various surfaces, can be very abundant in water bodies of temperate regions during springtime, as a result of buoyant oxygen bubbles produced by photosynthesis. Floating or drifting mats are rafts of green algae, including the filamentous *Spirogyra*

and diatoms, along with *Cyanobacteria* and bacteria (Burne *et al.*, 2014).

Both prokaryotes and eukaryotes produce extracellular polymeric substances (EPS), or simply exopolymers, which comprise negatively charged functional groups (for example, carboxyl and hydroxyl groups) with the ability of binding metal ions from the surrounding solution (Braissant *et al.*, 2007). The binding of Mg^{2+} and Ca^{2+} is crucial to enhance the precipitation of so-called microbial carbonates, especially dolomite. This mineral is scarce in modern sedimentary systems, although abundant in ancient rocks and its formation is a long-standing enigma (Vasconcelos *et al.*, 1995). Although numerous investigations of microbial dolomite have been made, the barriers that prevent the formation of ordered Mg-carbonates (i.e. dolomite and magnesite) under ambient conditions are still a matter of controversy (Machel, 2004; Xu *et al.*, 2013; Gregg *et al.*, 2015). It is suggested that microbial dolomite formation is aided by different groups of heterotrophic bacteria that foster the precipitation of dolomite through the supersaturation of solutions with respect to the carbonate (Vasconcelos *et al.*, 1995; Sánchez-Román *et al.*, 2008; Roberts *et al.*, 2013; Sanz-Montero *et al.*, 2019). In the presence of saturated solutions, the EPS excretions may act as a template for the extracellular nucleation of carbonates (Bontognali *et al.*, 2012; Krause *et al.*, 2012; Roberts *et al.*, 2013; Sanz-Montero *et al.*, 2019). Alternatively, Nash *et al.* (2011, 2019) drew attention to the occurrence of intracellular protodolomite and magnesite in coralline algae, and suggested that dolomite mineralization could be driven by Mg-rich polysaccharides at the cell perimeter of algae. Along the same lines, Anadón *et al.* (2002) provided evidence for high magnesian calcite (HMC) precipitation within oogonial cells of lacustrine charophytes.

As with dolomite, there is evidence that the nucleation of baryte may be improved by microbes and organic substances (EPS) in modern settings (Bonny & Jonnes, 2007; García del Cura *et al.*, 2014). Baryte can also form as biominerals in green algae such as *Spirogyra* (Kreger & Boere, 1969) and Desmids (Krejci *et al.*, 2011). The association of dolomite with accessory, but ubiquitous, baryte had been reported in lacustrine sedimentary rocks, where the dolomite and baryte could be primary minerals and biotic in origin (Sanz-Montero *et al.*, 2008, 2009). In contrast to ancient examples, the natural occurrences of the mineral assemblage comprised of Mg-rich carbonates, especially dolomite, and baryte in modern alkaline lakes are much less common. Thus, the mechanisms involved in the precipitation of this dolomite-bearing mineral association are still poorly understood. One of the few modern, lacustrine environments where the precipitation of dolomite occurs, is in the seasonal lake Caballo Alba, located in a closed wetland in Central Spain (Cabestrero & Sanz-Montero, 2018; Sanz-Montero *et al.*, 2021).

Using textural, mineralogical, geochemical and sedimentary characterization techniques, the authors aimed to study the mechanisms of precipitation of dolomite and the associated minerals in the algal mats developed in the highly alkaline lake Caballo Alba. The study shows that well-ordered dolomite crystals and magnesian calcite occur as inclusions within the filaments of *Spirogyra*. This work provides a framework for understanding lithification processes of the algal mats and gives evidence of a new way of dolomite biomineralization.

GEOLOGICAL SETTING

Lake Caballo Alba is located in an endorheic wetland (41°14′38.6″N//4°36′22.9″W) in the south-western sector of Duero Basin (Central Spain) (Fig. 1). Situated at an elevation of 768 masl (metres above sea level), the water basin overlies horizontally-bedded Miocene deposits of the Duero Basin. Caballo Alba, with a maximum area of 0.17 km^2 and is mainly a groundwater fed, shallow basin up to 0.5 m deep (Sanz-Montero *et al.*, 2021). In addition, low inputs of water derive from a small and extremely intermittent stream. The region is characterized by a continental climate, with low mean annual rainfall of 400 to 500 $mm \cdot year^{-1}$; with maximum values in November and minimum values in August. The annual average temperatures of 13°C with extreme values of −10°C and 38°C are registered in January and July (Sanz-Montero *et al.*, 2013; Cabestrero & Sanz-Montero, 2018). During springtime, the lake hosts benthic microbial mats that expand over the lake. The lake is also colonized by charophytes and the associated biota of ostracods. From June to October, coinciding with periods of low precipitation, the lake floor dries out and Caballo Alba becomes a playa covered by a white mineral crust (Fig. 1B). The crust contains an assemblage of authigenic carbonates (for

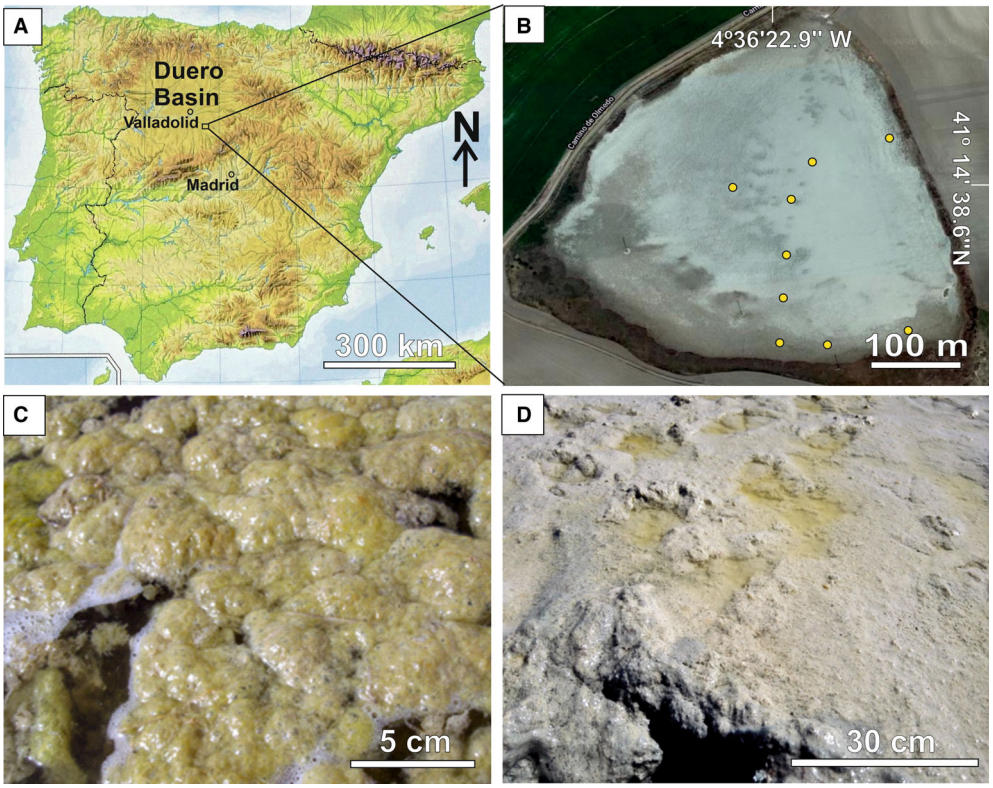

Fig. 1. (A) Location of lake Caballo Alba in the Duero Basin, Spain. (B) Satellite image of the playa Caballo Alba showing white minerals on the lake floor. Yellow circles indicate location of the studied samples. (C) Close-up view of the suspended algal mats in springtime. (D) Extensive white microbial mats developed on the floor. Notice that small brine pools formed in duck footprints.

example, calcite, dolomite, nesquehonite, hydromagnesite, natron and trona), sulphates (for example, hexahydrite, starkeyite, gypsum, thenardite and bloedite), chlorides (halite) and Mg-clays (Cabestrero & Sanz-Montero, 2018; Sanz-Montero *et al.*, 2021).

MATERIALS AND METHODS

Sample collection

The lake Caballo Alba was studied systematically between December 2011 and April 2021 in order to better understand the interactions between the sedimentary environment and the microbial mats hosted in the lake. This study is mainly based on data and observations taken in autumn and spring between 2016 and 2021, when benthic and suspended algal mats carpeted the bottom of the lake and water surface (Fig. 1). To carry out textural and mineralogical analyses, samples of the mats (0–3 cm depth) were collected from different sites, including the floor and suspended mats (Fig. 1C and D). In addition, two undisturbed sediment cores (up to 15 cm in depth) were collected with sampling tubes. For comparison, the mineralized mats recovered in July 2020 when the lake dried and converted into a playa were also analysed (Fig. 1B).

Physicochemical properties, hydrochemistry and hydrogeochemical modelling

Water samples were collected from the same location as the sediment samples wherever possible. Physicochemical parameters of the water column included the salinity (S), temperature (T), dissolved oxygen (DO), oxidation reduction potential (ORP) and pH values were recorded with a portable water multiparameter probe (Hanna Instruments 9828; Hanna Instruments, Woonsocket, RI, USA). The water samples were filtered under vacuum conditions using 0.45 μm pure cellulose acetate filters. Major cations (i.e. Ca^{2+}, K^{+}, Mg^{2+} and Na^{+}) and anions (i.e. Br^{-},

Cl^-, F^-, NO_2^-, NO_3^-, PO_4^{3-} and SO_4^{2-}) were analysed by ion chromatography, using METROHM 940 Professional IC Vario chromatograph (measuring range of conductivity detector: 0–15 000 μS cm^{-1}; Metrohm AG, Herisau, Switzerland). Major cations dissolved and Si concentration were analysed by ICP-AES carried out on a Spectro ARCOS (SPECTRO Analytical Instruments GmbH, Kleve, Germany) at Unidad de Técnicas Geológicas (UCM). The carbonate alkalinity (CO_3^{2-} and HCO_3^-) of the water was determined by titration. The solution was titrated with 0.1 N HCl added stepwise in 100 ml increments. The pH was recorded until pH 3 was reached using a Hanna pH 211 Microprocessor Meter (Hanna Instruments, Leighton Buzzard, UK). The standard titration analyses were made with Hamilton 20.2 as reference material. With the aim of calculating ion activities and saturation indices (SI) for most of the minerals present in the mats, hydrogeochemical modelling of overlying water was done using PHREEQC software by applying Debye-Hückle equations and IInl database (Cabestrero *et al.*, 2018).

Bulk mineralogy of microbial sediments (X-ray diffraction)

The mineralogy of the samples was examined through random powder X-ray diffraction (XRD) analysis using a Bruker D8 Advance diffractometer with Cu Kα radiation ($\lambda = 1.54060$Å) and equipped with a Sol-X detector (Bruker, Billerica, MA, USA). The samples were scanned from 2 to 65° 2θ with a step size of 0.02° 2θ and a counting time of 0.5 s per step. In the case of non-purified EPS, the counting time per step was 3 s. EVA Bruker software was used for XRD interpretation.

Location and identification of mineral inclusions (optical microscopy and staining)

Specimens of *Spirogyra* were laid out onto the herbarium paper and pressed for a week. Observation and photomicrography of bulk specimens were performed using an Olympus BX51 (Olympus Corporation, Tokyo, Japan). Microscopical observations allowed the identification of the filamentous green algae *Spirogyra* (Zygnematophyceae, Chlorohpyta) as the major constituent of the algobacterial mats. This was classified as *Spirogyra varians* (John *et al.*, 2002) by measuring the length and the width of the ellipsoidal zygospores and the width of filaments with a single chloroplast. Birefringent cellular inclusions were observed in a variety of locations within the filaments of living algae. For distinguishing calcium oxalate from other calcium-bearing minerals and between carbonate minerals (Dickson, 1965; Tucker & Wright, 1990), a combination of Alizarin red-S with potassium ferricyanide stains (at pH of 4) was applied. Then, specimens were placed in 5% acetic acid for 30 min to dissolve calcium carbonate and phosphate, but not oxalate (Pueschel, 2001).

Sedimentological textural features (SEM and ultrathin slices for TEM)

Textural features and mineral assemblages were established by scanning electron microscopy using images recorded with secondary and backscattered electrons, and energy dispersive X-ray systems (EDX). Some freshly fractured surfaces of representative samples were air-dried and coated with Au under vacuum conditions. Scanning electron microscopy observations were performed using a FEI INSPECT microscope (FEI Company, Hillsboro, OR, USA) for environmental electron microscopy (ESEM) equipped with an OXFORD INSTRUMENTS solid-state EDX detector (Oxford Instruments, Abingdon, UK), operating at 30 kV and low vacuum mode.

Two samples of suspended mats were fixed using the Karnovsky method. The material was stained by 1% of Osmium Tetraoxide. LR-white resin solution was added to embed the cells. The ultrathin slices were cut at 60 to 90 nm using a Leica Ultracut-e ultramicrotome (Leica Microsystems, Wetzlar, Germany). Samples were post-stained with uranyl acetate and lead citrate. Then, samples were analysed by a transmission electron microscope (JEOL JEM 1400; JEOL, Tokyo, Japan), operated at 40 to 120 kV and a point-to-point resolution of 0.38 nm at Centro Nacional de Microscopia Electrónica (CNME).

Extracellular polymeric substances extraction, purification and characterization (XRD/FT-IR/ICP-AES)

The EPS of mats collected in April 2018 were extracted, purified and characterized. The samples were mixed with deionized water (1:1, water: EPS) and filtered using 45 μm nitrocellulose. The filtrate was centrifuged in an Eppendorf 5810 R centrifuge (Eppendorf, Hamburg, Germany) for 10 min at 2500 RPM at 4°C. The supernatant was precipitated using three

volumes of ice-cold ethanol (96%) per volume of filtrate during 24 h at 4°C. The precipitate was recovered by centrifugation (6000 RPM for 10 min) and freeze-dried during 24 h in a Telstar Cryodos device (Telstar Industrial S.L., Terrassa, Spain).

The EPS were purified by dialysis: 0.10 g of freeze-dried powdered EPS was dissolved in 10 mL deionized water by adding 1 ml of 1 M HCl, in order to remove the carbonates and other soluble minerals, while stirring gently. The rehydrated material was placed into a dialysis bag (10 kDa), and dialyzed three times against 1 mM of EDTA for 24 h each time at 4°C. For the final dialysis step, deionized water was used, repeated three times for 24 h. Non-purified EPS sample was characterized by powder XRD (X-ray diffraction), FT-IR (Fourier transform – infrared spectroscopy) and ICP-AES (inductively coupled plasma – atomic emission spectrometry). For XRD analyses the same procedure described above was implemented. FT-IR analyses were carried out using 2 mg of sample that was mixed with 200 mg of dried KBr and subjected to a pressure of 10 ton·cm^{-2} during 10 min. Purified-EPS was also analysed by mixing 4 mg of freeze-dried sample with 85 mg of KBr. The FT-IR was recorded in the 4000 to 400 cm^{-1} range on a NICOLET NEXUS 670–680 spectrometer (Thermo Fisher Scientific, Waltham, MA, USA). The analysis of major and trace elements attached to non-purified EPS were carried out by ICP-AES on a SPECTRO ARCOS at Unidad de Técnicas Geológicas (UCM).

Characterization of carbonate minerals (TEM-AEM/SAED/HRTEM)

Transmission electron microscopy (TEM) observations and quantitative analyses of two representative samples of mats were obtained from powdered portions prepared using C-coated Cu grids. The TEM data were obtained using a JEOL JEM 2100, operated at 200 kV and a point-to-point resolution of 0.25 nm. Quantitative analyses by analytical electron microscopy (AEM) of particles were obtained in STEM mode with an OXFORD INSTRUMENTS EDX microanalysis system. Selected area electron diffraction (SAED) and high resolution transmission electron microscopy (HRTEM) images were used to determine the degree of ordering of carbonates. Indexation of d-spaces in the reciprocal space and HRTEM images were done using American Mineralogist Crystal Structure Database tables.

RESULTS

Mineralogy of sediments

The studied microbial mats consisted of a mineral assemblage that included up to 25% of the carbonates calcite ($CaCO_3$), high magnesian calcite (HMC) and dolomite ($CaMg(CO_3)_2$), minor baryte ($BaSO_4$) and silicates (i.e. phyllosilicates, quartz and feldspars) (Table 1 and Fig. S1). Minor quantities of magnesite ($MgCO_3$) and huntite ($CaMg_3(CO_3)_4$) were also recorded in the mats. In addition to these minerals, the whitish microbialites that cover the dry lake bed in summer (Fig. 1B) contained up to 65% of hydromagnesite ($Mg_5(CO_3)_4(OH)_2{\cdot}4H_2O$), northupite ($Na_3Mg(CO_3)_2$ Cl), halite (NaCl) and thenardite (Na_2SO_4) (Table 1). Occasionally, gypsum ($CaSO_4{\cdot}2H_2O$) was also detected by XRD in two core samples.

Overall, dolomite persistently had lower abundance than calcite (Fig. S1). The proportion of these phases remained relatively constant with depth (Table 1).

Physicochemical properties, hydrochemistry and hydrogeochemical modelling

Lake Caballo Alba presented high pH values of between 9.0 and 10.4 with brackish to salty water (1–16 g l^{-1}). The lowest pH and highest salinity values in the lake were measured in March 2017 (Table 2), coinciding with episodes of high temperatures and precipitations lower than average. The maximum negative ORP values were recorded during March 2019 (−368.6 mV), which could point to processes of degradation coupled with high rates of microbial mat production (i.e. manifested by high rates of dissolved oxygen).

The ionic composition of water indicated a Na^+–Cl^-–(SO_4^{2-})–(HCO_3^-) water type (Table 2), which were within the range of variation reported by Cabestrero & Sanz-Montero (2018) and Sanz-Montero *et al.* (2021). The predominant cations were Na^+ and Mg^{2+}, which reached their maximum values of 4744 ppm and 348 ppm, respectively, coinciding with the highest values of Cl^-, HCO_3^-, CO_3^{2-} and SO_4^{2-} in March 2017 (Table 2). At the time, the concentration of Ca^{2+} was very low (1.3 ppm),

Table 1. X-ray diffraction (XRD) semiquantitative analyses of the minerals deposited in lake Caballo Alba. Calcite (Cc), dolomite (Dol), hydromagnesite (Hmg), magnesite (Mgs), northupite (Ntp), halite (Hl), gypsum (Gp), thenardite (The), quartz (Qz), feldspar (Fsp) and phyllosilicates (Phy).

Location	Samples	Cc	Dol	Hmg	Mgs	Ntp	Hl	Gp	The	Qz	Fsp	Phy
		%w/w										
Floor mats	CA-Nov16-1	5	5	10	–	–	–	–	–	30	15	35
	CA-Nov16-2	10	5	–	–	–	–	–	–	25	20	40
	CA-Nov16-3	10	5	–	–	–	–	–	–	40	15	30
	CA-My17-1	15	10	–	–	–	–	–	–	10	20	45
	CA-Ap18-1	10	5	–	–	–	5	–	–	40	20	20
	CA-Ap18-2	5	<5	–	–	–	–	–	–	55	20	20
	CA-Dec18-1	15	5	–	–	–	–	–	–	20	20	40
	CA-Dec18-2	15	5	–	–	–	–	–	–	15	20	45
	CA-Dec18-3	20	5	–	–	–	–	–	–	35	20	20
	CA-Jul20-1	5	<5	–	–	–	–	–	–	35	20	40
	CA-Ap21-1	10	10	–	–	–	–	–	–	10	20	50
		10	5	–	–	–	–	–	–	15	15	55
Suspended mats	CA-Ap18-3	10	5	–	–	–	–	–	–	5	10	70
	CA-Ap18-4	10	5	–	–	–	–	–	–	5	20	60
	CA-Ap21-3	10	5	–	–	–	–	–	–	5	15	65
Dried mats	CA-Mar17-1	5	5	20	–	5	10	–	30	5	10	10
	CA-Jul20-2	5	5	25	5	–	–	–	–	10	10	40
	CA-Jul20-3	10	5	20	<5	–	–	–	–	10	15	40
	CA-Jul20-4	10	5	–	<5	5	<5	–	–	20	30	30
	CA-Jul20-5	5	5	15	–	10	10	–	10	5	15	25
	CA-Jul20-6	10	5	–	5	–	5	–	–	15	20	40
	CA-Jul20-7	5	5	10	–	15	5	–	20	<5	10	30
Core 1	CA-S1-0-2	15	10	–	–	–	–	–	–	20	10	45
	CA-S1-2-4	10	10	–	–	–	–	–	–	20	10	50
	CA-S1-4-6	15	10	–	–	–	–	–	–	10	15	50
	CA-S1-6-8	15	10	–	–	–	–	–	–	10	15	50
	CA-S1-8-10	15	10	–	–	–	–	10	–	10	10	45
	CA-S1-10-12	15	10	–	–	–	–	<5	–	5	15	55
Core 2	CA-S2-0-2	10	5	–	–	–	–	–	–	40	25	20
	CA-S2-2-4	10	<5	–	–	–	–	–	–	40	30	20

accounting for the highest Mg^{2+}/Ca^{2+} ratio of the period (267.7 ppm). Values of minor anions dissolved in the water (F^-, Br^-, NO_2^-, NO_3^- and PO_4^{2-}) were below 10 ppm, and only F^- was consistently dissolved in the water (Table 2). In March 2019, the concentrations of Si in the solutions (1.16 ppm) were lower than in the pore water of the microbial mats (2.19 ppm), although slightly higher than in previous seasons (i.e. April and December 2018) but much lower than in April 2021 (2.6 ppm). The concentration of Mg^{2+} showed the opposite behaviour (Table 2), its concentration in pore water was almost half (111 ppm) of that of overlying water (273 ppm). According to PHREEQC modelling efforts, calcite, aragonite, dolomite, huntite, magnesite and hydromagnesite were supersaturated (i.e. positive saturation indices) whereas natron and nesquehonite were permanently undersaturated in surface waters (Table 3). In addition, the saturation indices were negative for halite and the sulphates gypsum and thenardite (Table 3).

Field description of microbial mats

In spring, macroscopic filamentous green algae of the genus *Spirogyra* (Zygnematophyceae) grow abundantly on the bottom of Caballo Alba, where they occur entangled with *Cyanobacteria* of the genus *Oscillatoria* and other filamentous green algae. These colonies trap gases and usually form free-floating mats in which *Spirogyra* is by far the major constituent on which epiphytic diatoms live attached. The most abundant filaments have been identified as *Spirogyra varians* by optical microscopy (Figs 2 and 3). *Spirogyra varians* contains one spiral chloroplast strand in each cell that reaches *ca* 50 μm

Table 2. Hydrochemical and physicochemical features in the lake and pore water (bold letters and numbers) in different seasons.

Site	Date	Water T (°C)	pH	DO (%)	S (g l^{-1})	ORP (mV)	Cl^- (ppm)	F^- (ppm)	Br^- (ppm)	NO_2^- (ppm)	NO_3^- (ppm)
Lake	Mar 17	24.0	9.0	79.3	16.0	31.6	4449 ± 500	2.6 ± 0.3	–	–	–
Lake	Apr 18	18.0	9.7	46.3	1.2	46.3	233 ± 12	1.1 ± 0.1	0.77 ± 0.04	0.49 ± 0.03	3.1 ± 0.3
Lake	Dec 18	7.5	10.4	35.7	3.5	−149.8	1118 ± 12	1.3 ± 0.1	3.7 ± 0.4	<0.1	<2.5
Lake	Mar 19	17.6	9.6	90.3	6.5	−368.6	–	–	–	–	–
Pore water	**Mar 19**	**–**	**–**	**–**	**–**	**–**	**1645 ± 165**	**2.1 ± 0.2**	**8.8 ± 0.9**	**–**	**<5**
Lake	Apr 21	16.2	9.8	122.8	1.9	−37	796 ± 80	2.2 ± 0.2	3.1 ± 0.3	–	<2.5

Site	Date	Ca^{2+} (ppm)	K^+ (ppm)	Mg^{2+} (ppm)	Si (ppm)	Na^+ (ppm)	PO_4^{3-} (ppm)	SO_4^{2-} (ppm)	CO_3^{2-} (ppm)	HCO_3^- (ppm)
Lake	Mar 17	1.3 ± 0.1	241 ± 24	348 ± 50	–	4744 ± 500	–	3945 ± 400	1388 ± 104	4885 ± 366
Lake	Apr 18	18 ± 2.0	28 ± 3	100 ± 10	0.51 ± 0.10	473 ± 47	<1	226 ± 23	181 ± 14	447 ± 34
Lake	Dec 18	<20	48 ± 5	110 ± 11	0.86 ± 0.09	1497 ± 150	<1	855 ± 86	548 ± 41	1253 ± 94
Lake	Mar 19	–	–	273 ± 27	1.16 ± 0.12	–	–	–	–	–
Pore water	**Mar 19**	**3.9 ± 0.4**	**58 ± 5**	**111 ± 11**	**2.19 ± 0.22**	**1616 ± 162**	**7.1 ± 0.7**	**1175 ± 118**	**–**	**–**
Lake	Apr 21	5.6 ± 0.6	77 ± 8	124 ± 12	2.6 ± 0.3	1089 ± 109	–	740 ± 74	424 ± 32	571 ± 43

(<) indicates unquantifiable low values. (–) not registered/analysed.

Table 3. Saturation indices of carbonate, sulphate and chloride minerals deposited in lake Caballo Alba. Positive saturation indices are in bold letters.

Mineral	Saturation indices		
	Mar 17	Apr 18	Dec 18
Aragonite	**0.37**	**1.35**	**1.55**
Calcite	**0.51**	**1.50**	**1.70**
Dolomite	**4.13**	**5.16**	**5.21**
Huntite	**4.89**	**5.86**	**5.32**
Hydromagnesite	**7.45**	**6.10**	**5.02**
Magnesite	**1.99**	**2.00**	**1.78**
Monohydrocalcite	−0.34	**0.66**	**0.90**
Natron	−3.29	−5.57	−3.74
Nesquehonite	−1.04	−1.04	−1.37
Halite	−3.49	−5.56	−4.44
Carnallite	−13.65	−17.14	−15.56
Gypsum	−3.29	−2.39	−2.18
Thenardite	−3.51	−6.17	−4.82

in diameter with a variable length (Figs 2 and 4). Within the chloroplast, the pyrenoids, which mediate photosynthetic CO_2 fixation in the alga, accumulate starch (Fig. 2A and B). The filaments are surrounded by a hyaline and gelatinous sheath of extracellular polymeric substances (EPS). Filaments of *Spirogyra* were observed during different stages of their life cycle, including the reproduction stage (Fig. 2C and D), during which conjugation tubes are used to transfer the content of one gametangium cell (male) to the adjacent cell (female) (Figs 3 and 4). In the latter, a zygote develops that is released after decay of the female filament (John *et al.*, 2002).

Characterization of the EPS

The composition of the purified EPS extracted from suspended mats developed in Caballo Alba in April 2018 was revealed by FT-IR spectra (Fig. 5A). Results were interpreted according to Conley (1972). These confirmed the abundance of sulphur-related functional groups, including S = O (1067 cm^{-1}) and –SO_2 (1133 cm^{-1}). Polyphosphates (poly-P) were identified at bands 907 cm^{-1} (P–O–P) and 1240 cm^{-1} (P = O). Besides, the group PO_4^{3-} was present at 987 $cm^{-1}$and P = S at 800 cm^{-1}. Carboxylic acids (R-COOH) were recorded at 1720 cm^{-1}; amides (I and II) were detected at 1653 and 1530 cm^{-1}, respectively. Amino groups were recorded in bands combined with OH^- bands (Fig. 5A). Less abundant functional groups embraced SiOH (827 cm^{-1}), COO^- (1387 cm^{-1}) and CH_2 (1453 cm^{-1}).

In contrast, the FT-IR spectrum of non-purified EPS after freeze-drying revealed the abundance of anionic groups. It detected bands of CO_3^{2-} for v_2 at 867 cm^{-1} and for v_3 at 1427 cm^{-1}

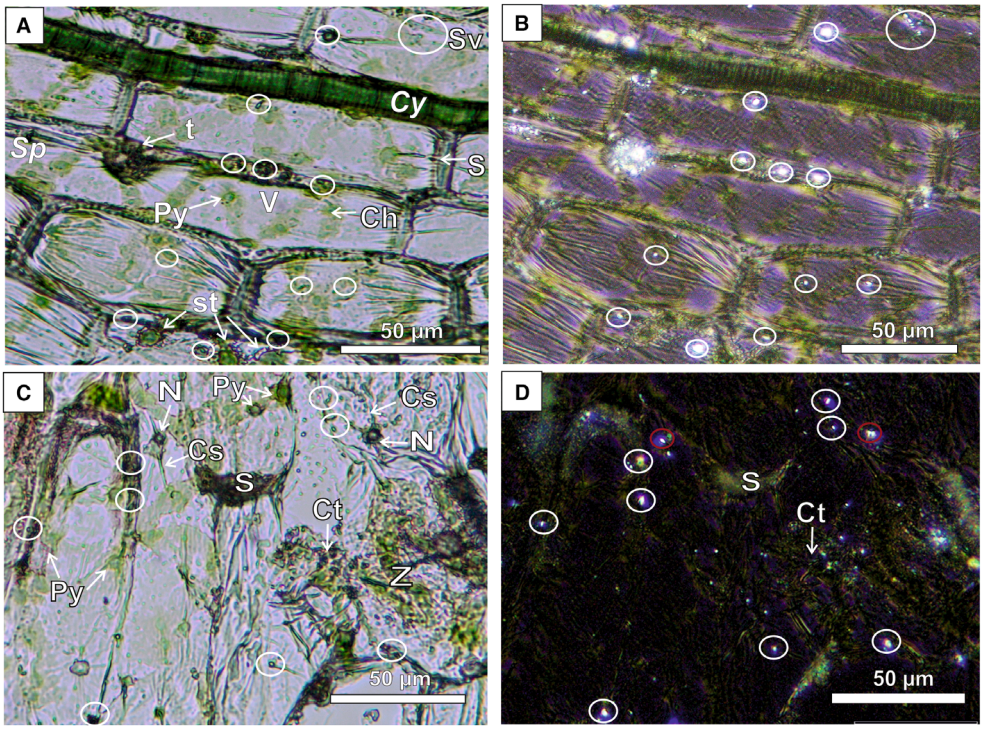

Fig. 2. Organic matter (OM) microphotographs under plane polarized light (A) and (C) and cross-polarized light nichols (B) and (D) of filaments of *Spirogyra* (*Sp*) containing highly birefringent carbonate inclusions (some encircled). (A) and (B) Vegetative filaments of *Spirogyra* associated with a *Cyanobacteria* (*Cy*) showing their typical features and mineral inclusions in different locations of the cells. Notice the green colour of many crystals and the presence of a thin and black coating around them. (C) and (D) Detail of reproductive cells in the process of conjugation. The two adjacent cells are joined by protuberances (conjugation tube). The content of one cell (male) passes into the other (inflated female cell) to form a zygote. Notice that the fusing contents contain carbonate inclusions. Labels: gelatinous cell wall (Cw), central vacuole (V), cell septa (S), spiral chloroplasts (Ch) suspended nucleus (N), cytoplasm strands (Cs), pyrenoids (Py), starch deposits (st), small vacuoles (Sv), cell protuberances and pores (t), conjugating tubes (Ct), zygote (Z).

(Fig. 5B). A strong band of HPO_4^{2-} for v_3 at 1067 cm^{-1} was also present. Peaks at 613 to 693 cm^{-1} corresponding to v_4 and v_3 at 1120 cm^{-1} were assigned to SO_4^{2-}. NO_3^- and NH_4^+ were represented by peaks at 800–833 cm^{-1} and 2933–2973 cm^{-1}, respectively. An Si–O stretching bond was identified at 987 cm^{-1}. O–H bending and stretching modes were visible at 1653 cm^{-1} and 3440 cm^{-1} wavenumbers, respectively. Overall, FT-IR analyses confirmed the abundance of carbonate, phosphate and sulphate in the cell dry mass of the algal mats (Fig. 5B). These compounds occurred as amorphous phases, as observed in the powder XRD diffractogram (Fig. S2).

The ICP-AES analyses of non-purified EPS revealed that divalent cations Ca^{2+} and Mg^{2+} were the most abundant elements (Table 4), although the concentration of Ca^{2+} was approximately double that of Mg^{2+}. An order of magnitude lower than those were the concentrations of Sr^{2+}, S^{6+}, K^+ and Na^+. Less abundant constituents were P^{4+}, Si^{4+}, Ba^{2+} and Mn^{2+}. Scarce $As^{3+,5+}$, Zn^{2+} and Li^+ were also concentrated in the EPS (Table 4).

Intracellular minerals in *Spirogyra*

Mineral inclusions, variable in number, size and location, were observed in living cells of *Spirogyra*, when examined with optical and electron microscopes (Figs 2, 3, 4 and 6). Crystalline inclusions were differentiated from other organic inclusions (pyrenoids, starch, among others) because they exhibited strong birefringence and different relief when examined under the polarizing microscope. Employing a combination of dyes allowed the identification of

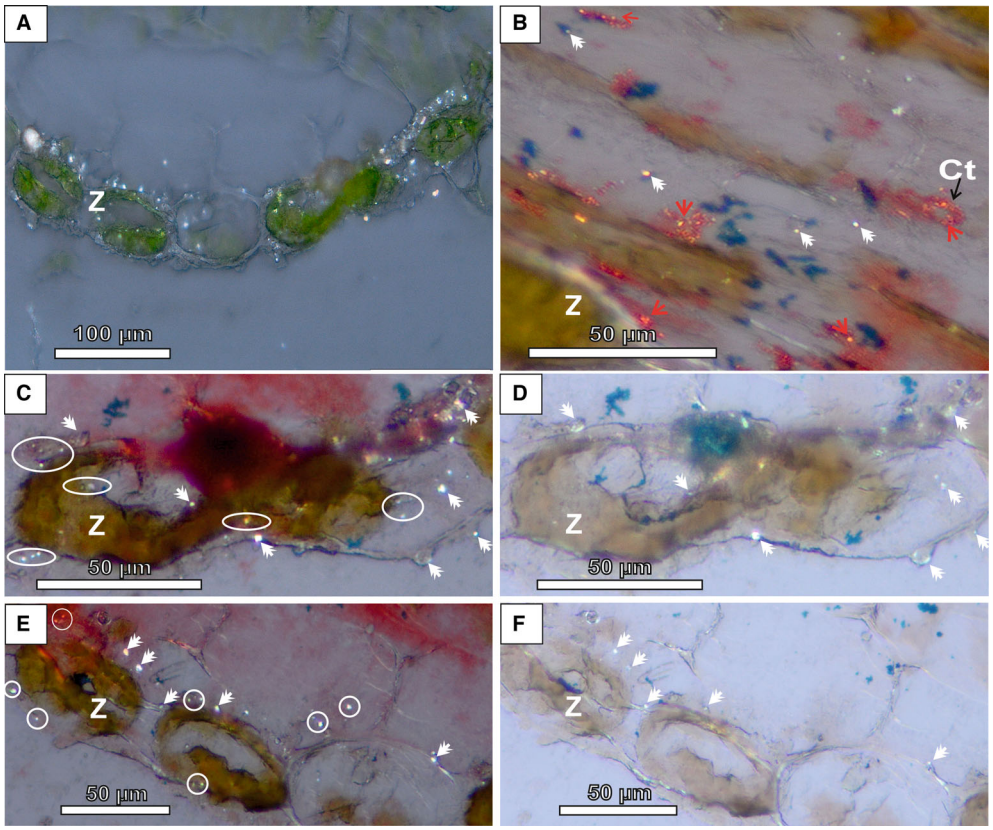

Fig. 3. Organic matter (OM) microphotographs under cross-polarized light nichols of intracellular crystals in filaments of *Spirogyra* bearing zygotes (Z). For distinguishing the mineralogy of inclusions, the filaments are stained with potassium ferricyanide and Alizarin red S (B) to (F) and then treated with 5% of acetic acid (D) and (F). (A) The thick and hyaline wall of the zygotes contains plenty of birefringent crystals. (B) The red dye allows visualization of the calcified elements of the cells including birefringent minerals attributable to calcite (red arrows). Dolomite (white arrows) and other mineralized components are blue or not stained. The crystals are associated with specialized vacuoles that tinted in red or blue. These occur in the conjugating tube (Ct), zygote walls (Z) and dispersed within the conjugating cells. (C), (D), (E) and (F) Prismatic to rhombohedral crystals that dissolved rapidly with acetic acid are indicated to be calcite (encircled). Unstained rhombohedral inclusions that survived treatment but were reduced in size are attributed to dolomite (double-headed white arrows).

intracellular Ca-rich minerals (i.e. carbonates or phosphates) that were stained intensely in red, whereas other associated crystals remained unstained. Stained and unstained inclusions were further identified as calcite and dolomite, respectively, by applying acetic acid (5%) that progressively dissolved the phosphates and carbonates (Fig. 3). X-ray diffraction analysis together with the combination of these two techniques confirmed the absence of calcium-oxalates, which are insoluble in acetic acid (Pueschel, 2001). The carbonate minerals were observed as green inclusions in different locations throughout the cells of the algae, including vegetative, healthy conjugating and gametangium cells, as well as in the cells that remained empty after conjugation (Figs 2 and 3). In addition, carbonate crystals were found outlining the mucilage of side-by-side filaments and the cell septa. Carbonates were very common around the outgrowth of protuberances developed in the cell walls, such as conjugation tubes and pores (Figs 3 and 4). They were also abundant in the thick mucilaginous wall of the mature zygospores, which typically contain abundant calcium as the red stain detected (Fig. 3).

Many inclusions accumulated in small vacuoles in parietal cytoplasm and in cytoplasmic strands that support the nucleus and connect adjoining cells (Figs 2, 3 and 4). The stains pigmented the specialized vacuoles in red or blue within the same cell, each embedding calcite or dolomite crystals (Fig. 3B). Viewed in ultrathin

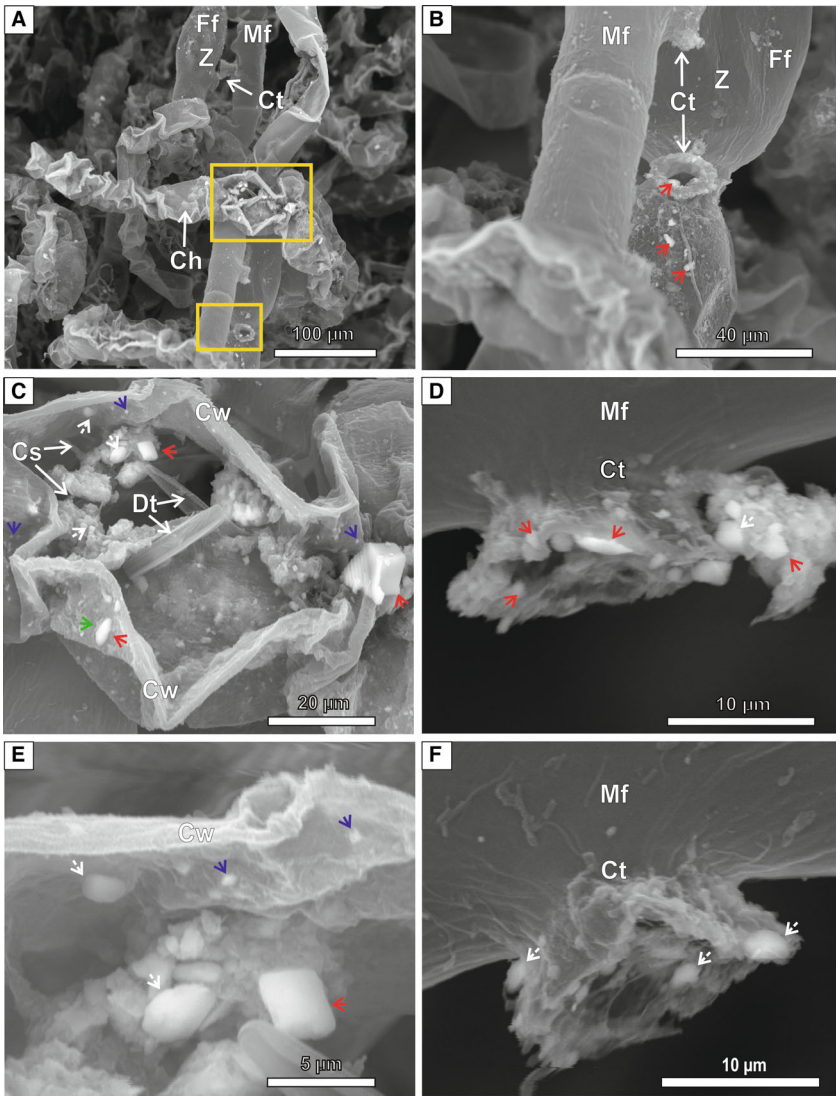

Fig. 4. Environmental electron microscopy (ESEM) photographs of carbonate accumulations in different filaments of *Spirogyra varians* (*Sp*). Carbonates contain variable Mg/Ca ratios, consistent with calcite (red arrows) and dolomite (white arrows). See energy dispersive X-ray (EDX) spectra of points labelled with a number in Fig. S3. (A) Carbonates accumulate abundantly around the conjugation tubes (Ct) and zygotes (Z) and in reproductive filaments (Ff and Mf), which are turgent. The intracellular carbonates and spiral chloroplasts (Ch) are seen as protuberances in shrunken and corrugated filaments. (B) Magnified view of a pair of filaments after conjugation. Notice carbonate crystals formed around the conjugation tubes (Ct) and the swollen female cells (Ff). (C) Magnified view of carbonate crystals attached to cytoplasm and chloroplast strands (Cs) within a shrunken cell, squared in (A). Different crystal forms are coexisting in the vicinity. A complex calcite crystal in the right shows a combination of spiral and rhombohedral morphologies. Another rice-shaped crystal of calcite lies in the wall (Cw) surrounded by remains of the mucilaginous sheath. Baryte crystals (blue arrows) are located on different sites of the cell walls. Notice the organic coating around a calcite crystal (green arrow). (D) Detail of an open conjugation tube in a male cell (Mf) containing dolomite and calcite crystals. (E) Magnified view of crystals shown in (C). (F) Dolomite crystals embedded within a conjunction tube.

sections by TEM, idiomorphic holes up to a size of 1 µm were evident in the cytoplasm (Fig. 6). A few holes contained remnants of minerals but most of them were empty because former grains had been likely pushed out during sectioning due to inadequate penetration of the resin in them or being dissolved during treatment (Kreger & Boere, 1969; Pueschel, 2001; Li *et al.*, 2016). The moulds left behind by crystals exhibited rhombic, rectangular or rice-grain habits and

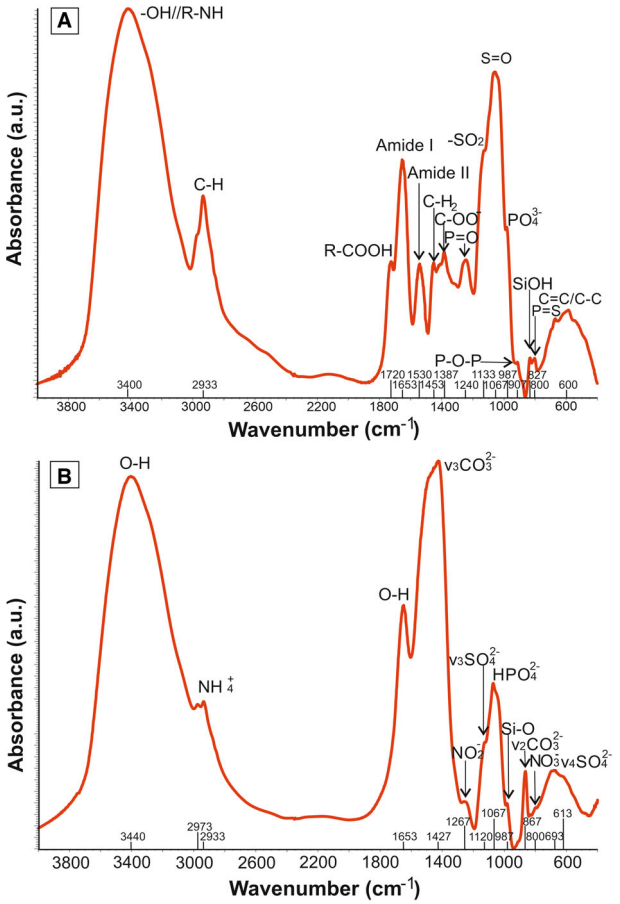

Fig. 5. Fourier transform – infrared spectroscopy (FT-IR) spectra of purified extracellular polymeric substances (EPS) (A) and non-purified EPS (B) of algal mats (See Fig. 1C for location).

commonly had curved surfaces (Fig. 6). The crystals developed irregular crystalline faces on their surfaces of attachment to organic substrates (Figs 6C and 7E). The crystal moulds were covered by a kind of membrane and/or enclosed by cytoplasmic material (Figs 6 and 7A). The presence of coatings and the range of forms and sizes of the moulds were coherent with the textures of numerous carbonate crystals identified by other techniques (Figs 2, 3, 4, 6 and 7).

The TEM/SEM–EDX analyses of carbonate inclusions detected variable Ca^{2+} and Mg^{2+} ratios (Table 5; Figs S1 and S3), consistent with co-occurrence of calcite and dolomite (Figs 4C to E and 7A to D). The association of carbonate crystals to strands, broken chloroplasts and other cellular remnants was clearly visible in shrunken cells (Figs 2, 3, 4 and 7). Many vegetative cells

Table 4. Inductively coupled plasma – atomic emission spectrometry (ICP-AES) analyses of non-purified extracellular polymeric substances (EPS) from lake Caballo Alba recovered in April 2018.

Element	Concentration (ppm)
Al	45 ± 5
As	<20
Ba	476 ± 48
Ca	70 300 ± 0.014
Fe	70 ± 7
K	2380 ± 0.42
Li	3
Mg	34 000 ± 0.03
Mn	148
Na	2300 ± 0.43
P	1728 ± 173
S	2400 ± 0.42
Si	853 ± 85
Sr	3785 ± 379
Zn	10

became corrugated as the mineralization of the internal components avoided the complete collapse of cells (Fig. 4C). It was observed that intracellular carbonates were further released into the extracellular environment as the sheaths enclosing them were removed, likely by the action of the microorganisms found in the vicinity (Fig. 7A). Through the transparent sheaths it could be seen that carbonate inclusions were covered by a kind of membrane (Fig. 7A). This coating was still evident in some extruded minerals, but in most of the latter the coverage was greatly reduced (Fig. 7D to F). Many of the extruded carbonates remained attached to the decaying sheaths, forming complex organo-mineral aggregates (Figs 4A to F, 7B and 7C).

Besides carbonates, it was observed that baryte crystals (up to 3 μm) occur persistently associated with the decaying filaments of *Spirogyra* (Figs 4C to E and 7C). Baryte appeared as scattered crystals or formed chains of aligned tabular crystals (Fig. 7C).

Concerning the composition of the *Spirogyra* sheaths enclosing the carbonates, EDX analyses detected Si^{4+}, Ca^{2+}, Mg^{2+}, Al^{3+}, K^{+}, Cl^{-}, S^{6+} and Na^{+}. Besides, P^{4+}, $Fe^{2+,3+}$ and Ba^{2+} occurred as minor constituents (Figs 7 and S3). Within the cells, the cytoplasm strands associated with the inclusions are enriched in S (Fig. 6B). In addition, they consisted of Si^{4+}, Al^{3+}, Mg^{2+}, K^{+}, P^{4+}, Na^{+}, $Fe^{2+,\ 3+}$ and Ca^{2+}.

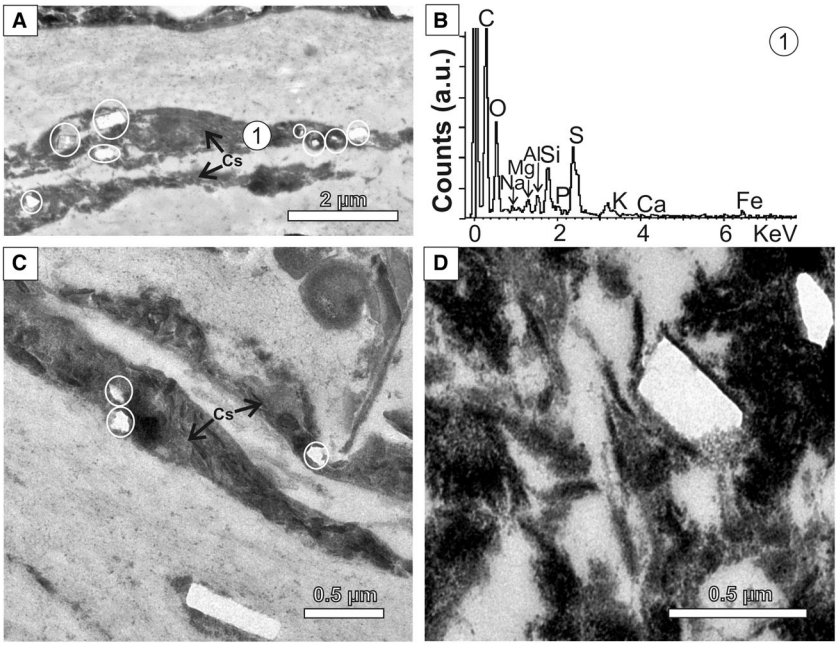

Fig. 6. Transmission electron microscopy (TEM) photographs of ultrathin sections. Idiomorphic holes correspond to minerals that have been pushed out during sectioning. (A) Long cytoplasmic strand (Cs) within a cell that contain several holes left by membrane-bounded crystals (encircled). Notice that some crystals are attached to the strand by an irregular face. (B) Energy dispersive X-ray (EDX) spectrum of spot labelled with '1'. (C) Loosely enclosed prismatic mould associated with crystal holes embedded in cytoplasm strands (encircled). (D) Moulds of two crystals embedded within organic components. One mould corresponds to an idiomorph crystal showing a kind of coating and an irregular face of attachment. The adjacent crystal shows curved faces.

Crystallo-chemical analyses of the carbonate crystals

The EDX analyses and SAED patterns further confirmed the presence of calcite and dolomite with a wide range of $CaCO_3$ and $MgCO_3$ molar ratios as percentage contents (Table 5) that displayed evidence of cation ordering (Figs 8 and 9). Some Ca-Mg crystals with $MgCO_3$ molar ratios as percentage contents ranging between 5% and 23% (Fig. 8E and F), were considered to be HMC, according to Tucker & Wright (1990). Other carbonates occurred as monocrystalline rhombohedra (500 nm–5 µm) (Figs 7E, 7F and 8A to D) and contained 32 to 54 $MgCO_3$ molar ratio as percentage contents (Table 5). SAED patterns revealed that these carbonates that deviate from dolomite stoichiometry display cation ordering (Fig. 8A to D). The super-lattice reflections: 101, 015, 021 and 113, characteristic of ordered dolomite structure (Gregg *et al.*, 2015), occurred in compositions with greater than *ca* 32 $MgCO_3$ molar ratio as percentage contents (Table 5; Fig. 8B). These fundamental reflections of dolomite were detected even in nanometric-sized rhombohedra (Fig. 8D). HRTEM images of these crystals (Fig. 9) reinforced the presence of the super-lattice reflection (015) along with other characteristic lattice fringes, corresponding to d-spacings of dolomite (i.e. 104, 110 and 006). The faces of some dolomite crystals exhibited smooth and well-defined rhombohedral edges (Fig. 9B), other surfaces were covered by carbonaceous coatings (Fig. 8A to C).

Up to 10 µm calcite crystals exhibited variable morphologies, including rhombohedral, rice-grain forms with their distinctive curved surfaces, and more complicated forms, which can coexist within a single cell (Figs 3, 4, 6, 7, 8E and 8F). SAED patterns showed that calcites are monocrystalline, irrespective of the crystal habit, size and Mg molar ratios as percentage contents (Fig. 8E and F).

The Ca-Mg carbonates analysed also contained Fe as a trace element, its concentration being higher in dolomite than in calcite (Table S1).

Besides HMC and dolomite, TEM analyses detected minor huntite and magnesite (Fig. 8G and H). They occurred as polycrystalline

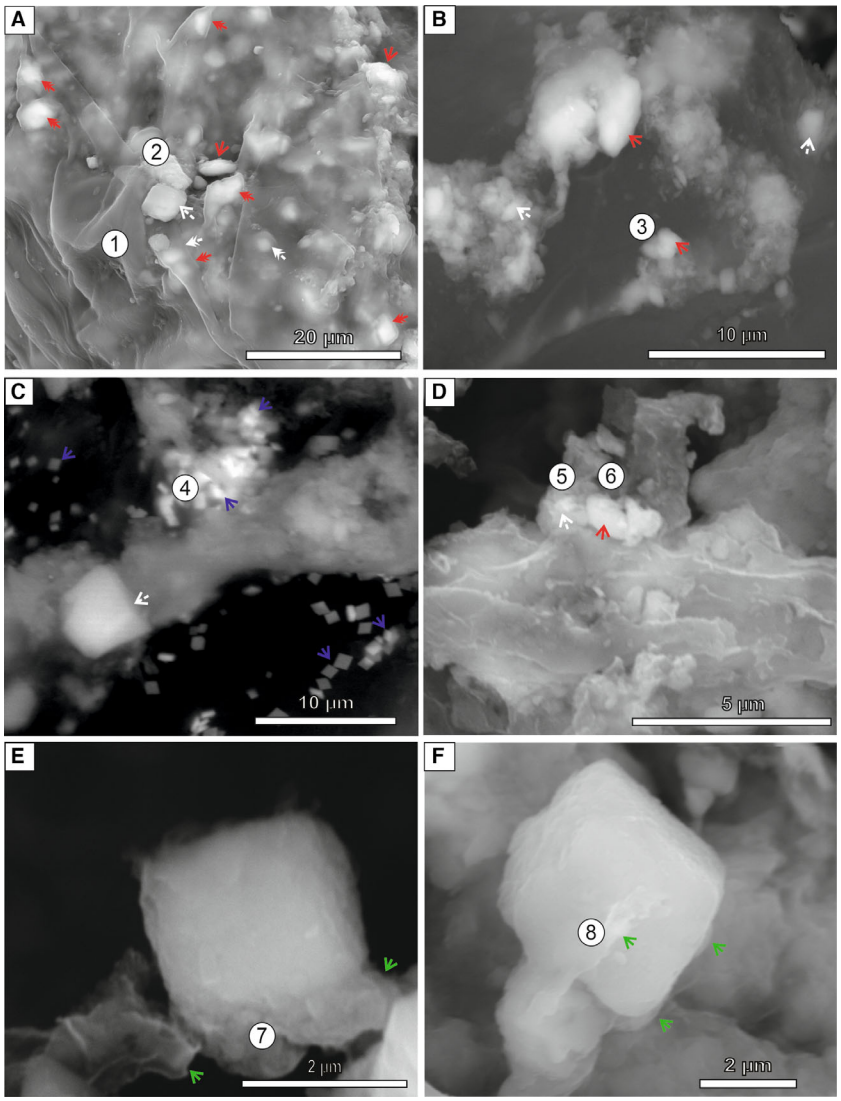

Fig. 7. Environmental electron microscopy (ESEM) microphotographs showing dolomite (white arrows), calcite (red arrows) and baryte crystals (blue arrows) associated with degraded filaments of *Spirogyra* (*Sp*). See energy dispersive X-ray (EDX) spectra of points labelled with a number in Fig. S3. (A) Intracellular carbonates are observed through the mucilaginous sheath of *Sp*. Some calcite and dolomite crystals are extruded into the extracellular environment through sheath breaches, more evident on the right side of the image. Notice that the carbonate inclusions are enclosed by their own coatings (double headed arrows). (B) Coiled remains of a cell encrusted by calcite and dolomite crystals. (C) Dolomite crystals attached to cellular remains are associated with tabular baryte accumulations. (D) Calcite and dolomite crystals included in a degraded filament. (E) Detail of a rhombic dolomite crystal attached to a decayed filament. (F) Magnified view of an extruded dolomite crystal exhibits remnants of an organic coating (arrowed).

nanometre-sized platy aggregates. SAED patterns revealed the presence of magnesite intergrowths in some huntite crystals (Fig. 8H).

DISCUSSION

The paper provides the first evidence of intracellular formation of ordered dolomite in the filamentous green alga *Spirogyra varians* (Zygnematales, Chlorophyta). *Spirogyra* is one of the dominant genera in continental water bodies and is used as a model organism to study the algal system worldwide (Lee, 2008); although few studies have focused on intracellular biomineralization in this alga (Barbosa *et al.*, 2022). Biomineralization processes are even less well-known in the colonies that proliferate in highly alkaline

Table 5. Transmission electron microscopy – analytical electron microscopy (TEM-AEM) analyses in molar ratios as percentage content (%mol) of carbonate minerals.

Crystal	$CaCO_3$ (mol%)	$MgCO_3$ (mol %)	Mineral Formula	Mineral
Fig. 8A	58	42	$Ca_{0.58}Mg_{0.42}(CO_3)_2$	Dolomite
Fig. 8B	68	32	$Ca_{0.68}Mg_{0.32}(CO_3)_2$	Dolomite
Fig. 8C	60	40	$Ca_{0.6}Mg_{0.4}(CO_3)_2$	Dolomite
Fig. 8D	64	36	$Ca_{0.64}Mg_{0.36}(CO_3)_2$	Dolomite
	62	38	$Ca_{0.62}Mg_{0.38}(CO_3)_2$	Dolomite
	61	39	$Ca_{0.61}Mg_{0.39}(CO_3)_2$	Dolomite
	57	43	$Ca_{0.57}Mg_{0.43}(CO_3)_2$	Dolomite
	56	44	$Ca_{0.56}Mg_{0.44}(CO_3)_2$	Dolomite
	54	46	$Ca_{0.54}Mg_{0.46}(CO_3)_2$	Dolomite
	46	54	$Ca_{0.46}Mg_{0.54}(CO_3)_2$	Dolomite
Fig. 8E	90	10	$(Ca_{0.90}Mg_{0.10})\ CO_3$	HMC
Fig. 8F	88	12	$(Ca_{0.88}Mg_{0.12})\ CO_3$	HMC
	95	5	$(Ca_{0.95}Mg_{0.05})\ CO_3$	HMC
	91	9	$(Ca_{0.91}Mg_{0.09})\ CO_3$	HMC
	89	11	$(Ca_{0.89}Mg_{0.11})\ CO_3$	HMC
	86	14	$(Ca_{0.86}Mg_{0.14})\ CO_3$	HMC
	85	15	$(Ca_{0.85}Mg_{0.15})\ CO_3$	HMC
	84	16	$(Ca_{0.84}Mg_{0.16})\ CO_3$	HMC
	80	20	$(Ca_{0.80}Mg_{0.20})\ CO_3$	HMC
	77	23	$(Ca_{0.77}Mg_{0.23})\ CO_3$	HMC

and Mg-rich lakes. This would explain why the ability of the genus *Spirogyra* to produce dolomite and HMC biominerals has passed unnoticed. Thereby, the intracellular precipitation of Mg-rich carbonates within *Spirogyra* of lake Caballo Alba seems to be a first example of a generalized process in similar water bodies. The occurrence of dolomite in *Spirogyra* is an important finding in the biotic formation of orderly dolomite.

As is common, *Spirogyra* filaments are mostly found forming floating mats in lake Caballo Alba. The intense photosynthetic activity of these mats results in high dissolved oxygen concentration in the lake that could be coupled with high rates of degradation of microbial and plant biomass, as manifested by negative ORP values (Table 2).

Depletion of PO_4^{3-} from the lake water of Caballo Alba is coherent with large amounts of HPO_4^{2-} anionic groups detected in EPS from the floating mats. Thereby, reflecting an effective phosphorous uptake from the environment and accumulation in the mats, some in the form of polyphosphate. Other electronegative anionic groups contained in the EPS such as CO_3^{2-}, SO_4^{2-} and others, are known to act as binding sites for the metals found in the solutions (i.e. Ca^{2+}, Mg^{2+}, Ba^{2+}, Sr^{2+}, K^+ and Na^+) (Braissant *et al.*, 2007). Mg/Ca ratios in the *Spirogyra* cells and carbonate inclusions, although variable, are much lower than in pore water and surface waters of the lake, which provides evidence of the preferential binding of Ca^{2+} over Mg^{2+} to the filaments and the involvement of the algae in changing the chemistry of the surrounding environment. Head *et al.* (2000) also described the ability of the large sulphur-oxidizing bacteria of the genus *Achromatium* of taking high amounts of Ca^{2+} from waters containing low concentrations of this element to form intracellular grains of carbonate. In addition, Martignier *et al.* (2016) reported an inverse relation between the abundance of cations concentrated in intracellular globules produced by some eukaryotes and the concentration of these in the surface waters of Lake Geneva. Notably, anionic groups of the non-purified EPS in Caballo Alba, occur as amorphous forms as observed through FT-IR spectra and XRD analyses of experimentally desiccated EPS. The lack of crystalline phases allows us to discard desiccation as a potential mechanism of crystallization of carbonates from amorphous precursors contained in EPS. Alternatively, optical and electron microscopical examinations provide strong evidence that dolomite and calcite grains nucleate intracellularly in different cells of *Spirogyra*. The accumulation of intracellular Ca^{2+} oxalates

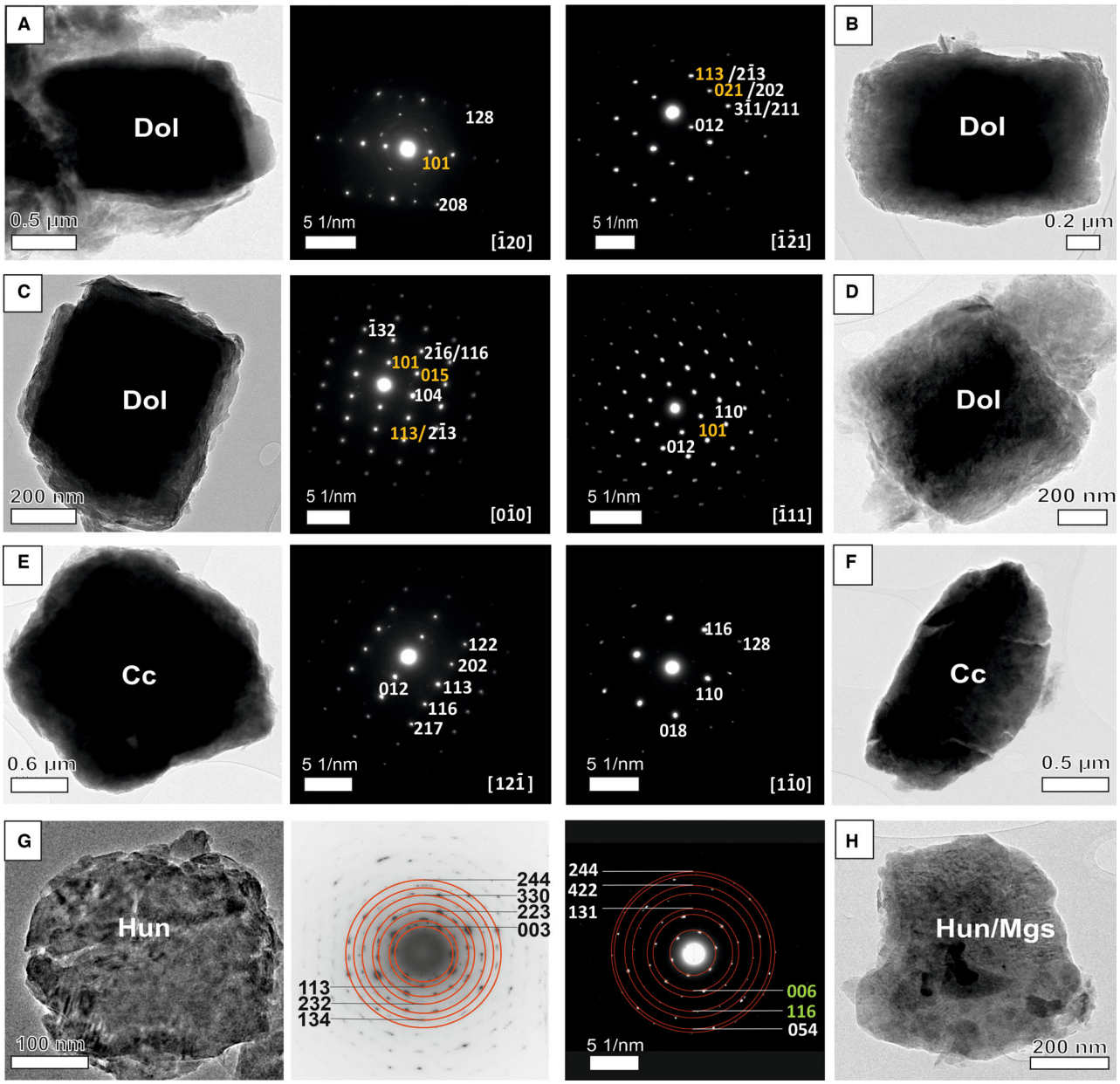

Fig. 8. Transmission electron microscopy (TEM) micrographs of Mg-Ca carbonate crystals. See the $MgCO_3$ contents in Table 5. (A) to (D) Nanometre-sized rhombs with their respective diffraction patterns revealing the presence of super-lattice reflections (labelled in yellow) and other reflections typical of dolomite (white labels). (E) and (F) Single crystals of high magnesian calcite (HMC) exhibiting rhombohedral and rice-grain morphologies and their diffraction patterns. (G) and (H) Flaky huntite aggregates. The concentric ring pattern of the diffraction spots reflect that they are polycrystalline aggregates. Selected area electron diffraction (SAED) patterns reveal discrete magnesite reflections (in green) among those corresponding to huntite.

(Pueschel, 2001) and less commonly aragonite (Mann *et al.*, 1988) and baryte (Kreger & Boere, 1969) in cells of *Spirogyra* had been long recognized (Klein, 1877, as cited in Pueschel, 2001), but it is the first time that intracellular dolomite, calcite and minor huntite–magnesite biomineralization has been documented for this alga. Differently, the production of monomineral carbonate inclusions has been described in phylogenetically distant microorganisms (Segovia-Campos *et al.*, 2021), including different members of the phyla *Cyanobacteria* (Couradeau

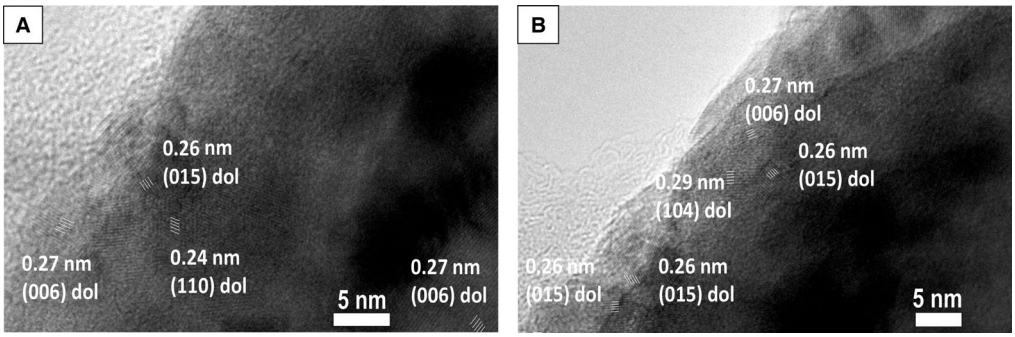

Fig. 9. (A) and (B) High resolution transmission electron microscopy (HRTEM) images of dolomite crystals showing (015) super-lattice fringes. The (006), (110) and (104) fringes, characteristic of dolomite, are also evident.

et al., 2012; Benzerara *et al.*, 2014; Popall *et al.*, 2020) and *Proteobacteria* (Monteil *et al.*, 2021) and in a microalga (Martignier *et al.*, 2016). Most of those inclusions consist of amorphous calcium carbonate phases that can contain other alkaline-earth metals (Segovia-Campos *et al.*, 2021). Even the widely known calcite inclusions of *Achromatium* are suggested to have an amorphous carbonate precursor (Head *et al.*, 2000). An increase in mineral ordering of the amorphous grains to produce calcite could occur upon bacteria death (Brasier *et al.*, 2018; Benzerara *et al.*, 2020). Amorphous phases of carbonates and polyphosphates, which are also thought to play a role in calcite biomineralization of eukaryotes and prokaryotes (Raven & Knoll, 2010; Li *et al.*, 2016), abound in the mats of Caballo Alba. However, there is no evidence that amorphous phases have acted as precursors for the formation of carbonates. Rather, electron diffraction patterns of crystals support that those accumulations in the algae of Caballo Alba are indeed ordered and occur as single crystals of HMC and dolomite (Table 5; Fig. 8). Otherwise, minor huntite and magnesite are polycrystalline and sometimes occur intermixed. The formation of orderly dolomite as a biomineral was confirmed by the presence of super-lattice reflections (i.e. 101, 015, 113 and 021) (Table 5; Fig. 8) (Tucker & Wright, 1990). Distinctive ordering reflections are consistently detected even in nanometre-sized crystals, which reinforces that individual formation of ordered dolomite and HMC is initiated intracellularly.

The SEM and TEM images provide evidence that the intracellular carbonates are coated by organic films (Figs 2, 3, 4 and 7). The occurrence of specialized compartments containing carbonate crystals within the cytoplasm of vegetative cells has been further highlighted using dyes (Fig. 3). Notably, some of these compartments contain Ca^{2+} and stain in red, like the calcite crystals they enclose. Other vacuoles in the vicinity, tinted in blue by the potassium ferricyanide dye, embrace dolomite crystals (Fig. 3). This dye reveals the distribution of ferrous iron in carbonates, staining Fe-bearing dolomite in blue (Dickson, 1965). Although to our knowledge this dye has not been previously tested in cytochemical studies, TEM and SEM–EDX analyses detect both $Fe^{2+,3+}$ in the organic cytoplasm and higher concentrations of Fe^{2+} in dolomite crystals than in calcite. Thereby, it seems reasonable to link the blue pigmentation of some organic compartments with the presence of Fe^{2+}. Curved surfaces, distinctive in many carbonate accumulations within *Spirogyra varians* (Figs 4D to F and 7A), provide additional evidence of crystal growth in reduced and mouldable compartments that delineate the shape of the forming crystals (Weiner & Dove, 2003).

Like in *Spirogyra varians*, Pueschel (2001) identified bounding coatings around cruciate calcium oxalate crystals in the alga *Spirogyra Hatillensis*. It is common in eukaryote microbes that calcium carbonate granules form within membrane-delimited vesicles, guided by enzymatic activity (Raven & Knoll, 2010). Organic membranes are implicated in the transport of cations, such as Ca^{2+} and Mg^{2+}, and $CO_3^{2-}/H^+/OH^-$ to the inner grains, thus controlling pH changes and minor and trace element composition (Head *et al.*, 2000; Weiner & Dove, 2003). The presence of magnesium within different compartments of the cells favours the formation and stability of internal carbonates in eukaryotes (Rodríguez-Blanco *et al.*, 2017). Organic coatings may also act as a nucleating template and

provide confinement within micrometre-sized compartments to carbonate biominerals favouring their stabilization and preventing their dissolution (Weiner & Dove, 2003; Benzerara *et al.*, 2020). Thereby, confinement in different specialized vacuoles containing variable proportions of ions (Ca^{2+}, Mg^{2+}, Mn^{2+} and Fe^{2+}) as detected by several techniques, could explain co-precipitation of calcite and dolomite as separate and individual crystals within the cells of *Spirogyra* from a similar extracellular solution, where Mg^{2+} highly exceeded Ca^{2+} concentrations.

Some crystals in *Spirogyra varian*s are attached to organic templates, which could direct nucleation of minerals by providing surface functional groups (Roberts *et al.*, 2013). Analogously, Nash *et al.* (2019) suggested that intracellular dolomite mineralization in coralline algae could be driven by Mg-rich polysaccharides at their cell perimeter. In coralline algae, protodolomite crystals are associated with magnesite, but polymineral biomineralization in green algae is uncommon. Anadón *et al.* (2002) provided an example of HMC and aragonite accumulations within single oogonial cells of the genus *Chara* (Chlorophyta). Unlike *Chara*, polymineral deposits are observed in a variety of cellular locations within the *Spirogyra* filaments, being especially abundant in reproductive cells and in newly formed zygotes. The wide distribution of inclusions could be a common feature in the genus *Spirogyra*, as Pueschel (2001) also reported the spatial association of oxalate crystals to all cells of *Spirogyra hatillensis*, except for zygotes. On basis of the cellular locations of oxalate crystals, Pueschel (2001) speculated that oxalate accumulation might have some relevance to reproduction in *Spirogyra* species, which promotes osmotic changes and alteration of the original cell walls during the formation of conjugation tubes. Along the same terms, Permann *et al.* (2021) documented that cell wall characteristics of *Maugeotia* spp. (*Zygnematophyceae*) change during sexual reproduction. Overall, the abundance of carbonate crystals in conjugating cells and zygospores of *Spirogyra varians* support that changes close in time to conjugation could favour the accumulation of carbonates. However, knowledge on the cell composition during conjugation in *Zygnematophyceae* is scarce because the induction of conjugation under laboratory conditions is difficult and was successful only in a few genera of *Spirogyra* (Permann *et al.*, 2021, and references therein). Different stress conditions lead to conjugation in *Spirogyra*. Specifically, under CO_2-limiting stress the photosynthetic activity of the algae is restricted (Holzinger & Karsten, 2013). To maintain photosynthesis, the alga induces a CO_2-concentrating mechanism for the uptake of extracellular inorganic carbon and increases CO_2 concentration in the pyrenoids (Wang *et al.*, 2003; Toyokawa *et al.*, 2020). The activation of this mechanism involves physiological changes of some green algae such as the formation of a starch sheath around the pyrenoids (Toyokawa *et al.*, 2020) and the relocation of low-CO_2 inducible proteins into the pyrenoids, as well as Ca^{2+}-bound to these proteins (Wang *et al.*, 2003).

Based on the distribution of the carbonate crystals around the starch-coated pyrenoids of the vegetative filaments of *Spirogyra varians*, the authors can only speculate that at low-CO_2 caused by desiccation, the CO_2 concentrating mechanisms tuned by the alga shortly before their reproduction, could play a role in intracellular carbonate precipitation. During the conjugation stage, the crystals together with the cell contents would be transferred to the zygotes through the conjugation tubes.

In addition to carbonates, the filaments of the algae provide sites for the nucleation of tabular baryte crystals. Overall, the production of elemental sulphur by the microbial consortium accounts for an appreciable concentration of S (2400 ppm) in the EPS and cytoplasm. The discrete precipitation of baryte around the alga walls could be further facilitated by the bioaccumulation of Ba^{2+} found in their cellular excretions. It is known that Ba^{2+} cations are absorbed to negatively charged sites on the algae walls (Krejci *et al.*, 2011). The ability of different genera of green algae (*Chlorophyta*), including *Spirogyra* and *Desmids*, to accumulate baryte within their cells have been reported by a number of authors (Kreger & Boere, 1969; Krejci *et al.*, 2011; Barbosa *et al.*, 2022). However, at this stage, the exact location of baryte crystals associated *in vivo* with the algal filaments has not been identified in Caballo Alba deposits. Future studies should aim at determining the emplacement of baryte crystals.

The microbial mats developed seasonally in a shallow, highly alkaline lake provide a new mechanism of formation of primary and ordered dolomite. Gregg *et al.* (2015) suggested that dolomite in modern depositional environments forms from very high magnesian calcite precursors. In Caballo Alba, the coeval formation of

calcite and dolomite occurs in a short period of time during the life of the algae, thus greatly reducing the possibility of these transformations proceeding. The relatively constant proportions of calcite and dolomite in buried sediment also argues against long-term reactions of transformation. Rather, these results suggest that microbial Mg-carbonates, including dolomicrite, have potential for preservation in the rock record. Good examples of lacustrine rocks containing this type of association have been reported in Cenozoic successions (García del Cura *et al.*, 2001; Sanz-Montero *et al.*, 2009). Considering that green algae related to *Spirogyra* could date back to the Palaeozoic, and that *Spirogyra* were especially abundant in the Cenozoic fossil record (Martín-Closas, 2003), these findings add a new perspective to the study of ancient lacustrine dolomites.

CONCLUSIONS

Until now, reports of intracellular biomineralization of carbonates in eukaryotes were mostly limited to calcite. This study provides the first evidence of intracellular biomineralization of magnesian carbonates, including ordered dolomite in natural microbial mats of the green filamentous alga *Spirogyra*. These filamentous algae form dense mats that develop seasonally in the highly alkaline and Mg-rich lake, Caballo Aba, in Central Spain. Orderly dolomite and high magnesian calcite crystals nucleate separately within vacuoles in a variety of cellular locations. Confinement in different specialized vacuoles could explain the co-occurrence of single calcite and dolomite crystals, some of them showing curved faces. The crystals occur attached to the organic surfaces that provide templates for the crystallization of the minerals. The variability in the style of carbonate biomineralization suggests that the alga do not strictly control the mineral they produce and may reflect the influence of the geochemical environment, such as the high availability of Mg^{2+} in the surface water. The ability of *Spirogyra* to accumulate Ba^{2+} may favour the association of baryte to their collapsed filaments. Further studies are needed to evaluate its possible intracellular precipitation.

This paper expands the range of producers and minerals nucleated intracellularly. Green alga related with *Spirogyra* appeared in the fossil record as early as the Early Palaeozoic and nowadays this genus is widespread in lakes. Therefore, these findings raised the importance of research into this new mechanism of dolomite biomineralization.

ACKNOWLEDGEMENTS

This research work has been funded by the Spanish Ministry of Economy and Competitiveness through National Research Projects CGL2015-66455-R (MINECO-FEDER and PID2021-123735OB-C22). This project is part of the scientific activities of Research Group UCM-910404. Dr Pablo del Buey acknowledges support from a Predoctoral Grant (CT27/16-CT28/16UCM). Dr Óscar Cabestrero is acknowledged for helping with hydrogeochemical modelling and Dr Esteban Urones for helping with indexation of d-spacing measured by SAED. We also thank Dr Tomás Gallardo for assistance in the classification of *Spirogyra*. The assistance provided by an anonymous reviewer and the associated editor Mike Rogerson is greatly appreciated.

CONFLICT OF INTEREST

We declare no conflict of interest.

AUTHOR CONTRIBUTIONS

Both authors contributed to study conception and design. PB carried out sampling, treatment and analyses with input from MESM. MESEM wrote the manuscript. PB contributed to reviewing and editing the manuscript.

DATA AVAILABILITY STATEMENT

Data available on request from the authors.

REFERENCES

Anadón, P., **Utrilla, R.** and **Vázquez, A.** (2002) Mineralogy and Sr-Nd geochemistry of charophyte carbonates: a new tool for paleolimnological research. *Earth Planet. Sci. Lett.*, **197**, 205–214.

Barbosa, N., **Jaquet, J.M.**, **Urquidi, O.**, **Adachi, T.B.N.** and **Filella, M.** (2022) Combined *in vitro* and *in vivo* investigation of barite microcrystals in *Spirogyra* (*Zygnematophyceae*, *Charophyta*). *J. Plant. Physiol.*, **276**, 153769.

Benzerara, K., **Bolzoni, R.**, **Monteil, C.**, **Beyssac, O.**, **Forni, O.**, **Alonso, B.**, **Asta, M.P.** and **Lefevre, C.** (2020) The

gammaproteobacterium Achromatium forms intracellular amophous calcium carbonate and not (crystalline) calcite. *Geobiology*, **19**, 199–213.

Benzerara, K., **Skouri-Panet, F.**, **Li, J.**, **Férard, C.**, **Gugger, M.**, **Laurent, T.**, **Couradeau, E.**, **Ragon, M.**, **Cosmidis, J.**, **Menguy, N.**, **Margaret-Oliver, I.**, **Tavera, R.**, **López-García, P.** and **Moreira, D.** (2014) Intracellular Ca-carbonate biomineralization is widespread in *Cyanobacteria*. *Proc. Natl. Acad. Sci. U. S. A.*, **111**, 10933–10938.

Bonny, S.M. and **Jonnes, B.** (2007) Barite ($BaSO_4$) biomineralization at Flybye springs, a cold Sulphur spring system in Canada's northwest Teritories. *Can. J. Earth Sci.*, **44**, 835–856.

Bontognali, T.R.R., **Vasconcelos, C.**, **Warthmann, R.J.**, **Lundberg, R.** and **Mckenzie, J.A.** (2012) Dolomite-mediating bacterium isolated from the shabkha of Abu Dabi (UAE). *Terra Nova*, **24**, 248–254.

Braissant, O., **Decho, A.W.**, **Dupraz, C.**, **Glunk, C.**, **Przekop, K.M.** and **Visscher, P.T.** (2007) Exopolymeric substances of sulfate-reducing bacteria: interactions with calcium at alkaline pH and implication for formation of carbonate minerals. *Geobiology*, **5**, 401–411.

Brasier, A., **Wacey, D.**, **Rogerson, M.**, **Guagliardo, P.**, **Saunders, M.**, **Kellner, S.**, **Mercedes-Martin, R.**, **Prior, T.**, **Taylor, C.**, **Matthews, A.** and **Reijmer, J.** (2018) A microbial role in the construction of mono Lake carbonate chimneys? *Geobiology*, **2**, 540–555.

Burne, R.V. and **Moore, L.S.** (1987) Microbialites: organosedimentary deposits of benthic microbial communities. *Palaios*, **2**, 241–254.

Burne, R.V., **Moore, L.S.**, **Christy, A.G.**, **Troitzsch, U.**, **King, P.L.**, **Carnerup, A.M.** and **Hamilton, P.J.** (2014) Stevensite in the modern thrombolites of Lake Clifton, Western Australia: a missing link in microbialite mineralization? *Geology*, **42**, 575–578.

Cabestrero, Ó. and **Sanz-Montero, M.E.** (2018) Brine evolution in two inland evaporative environments: influence of microbial mats in mineral precipitation. *J. Paleolimnol.*, **59**, 139–157.

Cabestrero, Ó., **Sanz-Montero, M.E.**, **Arregui, L.**, **Serrano, S.** and **Visscher, P.T.** (2018) Seasonal variability of mineral formation in microbial mats subjected to drying and wetting cycles in alkaline and hypersaline sedimentary environments. *Aquat. Geochem.*, **24**, 79–105.

Conley, R.T. (1972) *Infrared Spectroscopy*, 2nd edn, p. 355. Allyn and Bacon, Boston, MA.

Couradeau, E., **Benzerara, K.**, **Gérard, E.**, **Moreira, D.**, **Bernard, S.**, **Brown, G.E.** and **López-García, P.** (2012) An early-branching microbialite cyanobacterium forms intracellular carbonates. *Science*, **336**, 459–462.

Dickson, J.A. (1965) Modified staining technique for carbonates in thin section. *Nature*, **205**, 587.

Dupraz, C., **Reid, R.P.**, **Braissant, O.**, **Decho, A.W.**, **Norman, R.S.** and **Visscher, P.T.** (2009) Processes of carbonate precipitation in modern microbial mats. *Earth. Sci. Rev.*, **96**, 141–162.

García del Cura, M.Á., **Calvo, J.P.**, **Ordóñez, S.**, **Jones, B.F.** and **Cañaveras, J.C.** (2001) Petrographic and geochemical evidence for the formation of primary, bacterially induced lacustrine dolomite: La Roda "white earth" (Pliocene, Central Spain). *Sedimentology*, **48**, 897–915.

García del Cura, M.Á., **Sanz-Montero, M.E.**, **De los Ríos, M.A.** and **Ascaso, C.** (2014) Microbial dolomite in freshwater carbonate deposits. *Sedimentology*, **61**, 41–55.

Gregg, J.M., **Bish, D.L.**, **Kaczmarek, S.E.** and **Machel, H.G.** (2015) Mineralogy, nucleation and growth of dolomite in the laboratory and sedimentary environment: a review. *Sedimentology*, **62**, 1749–1769.

Head, I.M., **Gray, N.D.**, **Babenzien, H.D.** and **Glöckner, F.O.** (2000) Uncultured giant sulfur bacteria of the genus Achromatium. *FEMS. Microbial Ecol.*, **33**, 171–180.

Holzinger, A. and **Karsten, U.** (2013) Desiccation stress and tolerance in green algae: consequences for ultrastructure, physiological, and molecular mechanisms. *Front. Plant Sci.*, **4**, 1–18.

John, D.M., **Whitton, B.A.** and **Brook, A.J.** (2002) *The Freshwater Algal Flora of the Bristish Isles: An Identification Guide to Freshwater and Terrestrial Algae*, p. 702. Cambridge University Press, Natural History Museum, British Phycological Society, London.

Klein, J. (1877) Algologische Mittheilungen. *Flora*, **60**, 315–319.

Krause, S., **Liebetrau, V.**, **Gorb, S.**, **Sánchez-Román, M.**, **McKenzie, J.A.** and **Treude, T.** (2012) Microbial nucleation of Mg-rich dolomite in exopolymeric substances under anoxic modern seawater salinity: new insight into an old enigma. *Geology*, **40**, 587–590.

Kreger, D.R. and **Boere, H.** (1969) Some observations on barium sulphate in *spirogyra*. *Acta. Bot. Neerl.*, **18**, 143–151.

Krejci, M.R., **Wasserman, B.**, **Finney, L.**, **McNulty, I.**, **Legnini, D.**, **Vogt, S.** and **Joester, D.** (2011) Selectivity in biomineralization of barium and strontium. *J. Struc. Biol.*, **176**, 192–202.

Lee, R.E. (2008) *Phycology*, p. 547. Cambridge University Press, Cambridge.

Li, J., **Margaret-Olivier, I.**, **Cam, N.**, **Boudier, T.**, **Blondeau, M.**, **Leroy, E.**, **Cosmidis, J.**, **Skouri-Panet, F.**, **Guigner, J.M.**, **Férard, C.**, **Poinsot, M.**, **Moreira, D.**, **López-García, P.**, **Cassier-Chauvat, C.**, **Chauvat, F.** and **Benzerara, K.** (2016) Biomineralization patterns of intracellular carbonatogenesis in *Cyanobacteria*: molecular hypothesis. *Minerals*, **6**, 1–21.

Machel, H.G. (2004) Concepts and models of dolomitization: a critical reappraisal. In: *The Geometry and Petrogenesis of Dolomite Hydrocarbon Reservoirs* (Eds Braithwaite, C.J.R., Rizzi, G. and Darke, G.), *Geol. Soc. London, Spec. Publ*, **235**, 7–63.

Mann, S., **Mann, H.** and **Fyfe, W.S.** (1988) Intracellular aragonite crystals in the fresh-water alga, spirogyra sp. *Mineral. Mag.*, **52**, 241–245.

Martignier, A., **Pacton, M.**, **Filella, M.**, **Jaquet, J.M.**, **Barja, F.**, **Pollok, K.**, **Langenhorst, F.**, **Lavigne, S.**, **Guagliardo, P.**, **Kilburn, M.R.**, **Thomas, C.**, **Martini, R.** and **Ariztegui, D.** (2016) Intracellular amorphous carbonates uncover a new biomineralization process in eukaryotes. *Geobiology*, **15**, 240–253.

Martín-Closas, C. (2003) The fossil record and evolution of freshwater plants: A review. *Geol. Acta*, **1**, 315–338.

Monteil, C.L., **Benzerara, K.**, **Menguy, N.**, **Bidaud, C.C.**, **Michot-Achdjian, E.**, **Bolzoni, R.**, **Mathon, F.P.**, **Coutaud, M.**, **Alonso, B.**, **Garau, C.**, **Jézéquel, D.**, **Viollier, E.**, **Ginet, N.**, **Floriani, M.**, **Swaraj, S.**, **Sachse, M.**, **Busigny, V.**, **Duprat, E.**, **Guyot, F.** and **Lefevre, C.T.** (2021) Intracellular amorphous Ca-carbonate and magnetite biomineralization by a magnetotactic bacterium affiliated to the Alphaproteobacteria. *ISME J.*, **15**, 1–18.

Nash, M.C., **Diaz-Pulido, G.**, **Harvey, A.S.** and **Adey, W.** (2019) Coralline algal calcification: A morphological process-based understanding. *PLosOne*, **14**, e0221396.

Nash, M.C., **Trotzsch, U.**, **Opdkye, B.N.**, **Trafford, J.M.**, **Russell, B.D.** and **Kline, D.I.** (2011) First discovery of dolomite and magnesite in living coralline algae and its geobiological implications. *Biogeosciencies*, **8**, 3331–3340.

Permann, C., **Herburger, K.**, **Niedermeier, M.**, **Felhofer, M.**, **Gierlinger, N.** and **Holzinger, A.** (2021) Cell wall characteristics during sexual reproduction of *Mougeotia sp.* (*Zygnematophyceae*) revealed by electron microscopy, glycan microarrays and. *RAMAN Spect.*, **258**, 1261–1275.

Popall, R.M., **Bolhuis, H.**, **Muyzer, G.** and **Sánchez-Román, M.** (2020) Stromatolites as biosignatures of atmospheric oxygenation: carbonate biomineralization and UV-C resilience in a *Geitlerinema* sp.-dominated culture. *Front. Microbiol.*, **11**, 1–17.

Pueschel, C.M. (2001) Calcium oxalate crystals in the green alga spirogyra Hatillensis (Zygnematales, Chlorophyta). *Int. J. Plant. Sci.*, **162**, 1337–1345.

Raven, J.A. and **Knoll, A.H.** (2010) Non-skeletan biomineralization by eukaryotes: matters of moment and gravity. *J. Geomicrobiol.*, **27**, 572–584.

Roberts, J.A., **Kenward, P.A.**, **Fowle, D.A.**, **Goldstein, R.H.**, **González, L.A.** and **Moore, D.S.** (2013) Surface chemistry allows for abiotic precipitation of dolomite at low temperature. *Proc. Natl. Acad. Sci. U. S. A.*, **110**, 14540–14545.

Rodríguez-Blanco, J.D., **Sand, K.K.** and **Benning, L.G.** (2017) ACC and Vaterite as intermediates in the solution-based crystallization of CaCO3. In: *A New Perspectives on Mineral Nucleation and Growth* (Eds Van Driessche, A.E.S., Kellermeier, M., Benning, L.G. and Gebauer, D.), p. 380. Springer, Cham.

Sánchez-Román, M., **Vasconcelos, C.**, **Schmid, T.**, **Dittrich, M.** and **McKenzie, J.A.** (2008) Aerobic microbial dolomite at the nanometer scale: implications for the geologic record. *Geology*, **36**, 879–882.

Sanz-Montero, M.E., **Arroyo, X.**, **Cabestrero, Ó.**, **Calvo, J.P.**, **Fernández, E.**, **Fidalgo, C.**, **García del Cura, M.Á.**, **García-Avilés, J.**, **González, J.A.**, **Rodríguez-Aranda, J.P.** and **Rovira, J.V.** (2013) Procesos de sedimentación y biomineralización en la laguna alcalina de Las Eras (Humedal Coca-Olmedo). *Geogaceta*, **53**, 97–100.

Sanz-Montero, M.E., **Cabestrero, Ó.** and **Sánchez-Román, M.** (2019) Microbial Mg-rich carbonates in an extreme alkaline Lake (las eras, Central Spain). *Front. Microbiol.*, **10**, 148.

Sanz-Montero, M.E., **Rodríguez-Aranda, J.P.** and **Del Buey, P.** (2021) Influencia del sustrato cenozoico en el origen y sedimentación de la laguna hiperalcalina de Caballo Alba (Segovia). *Geogaceta*, **70**, 31–34.

Sanz-Montero, M.E., **Rodríguez-Aranda, J.P.** and **García del Cura, M.Á.** (2008) Dolomite-silica stromatolites in Miocene lacustrine deposits from the Duero Basin, Spain: the role of organotemplates in the precipitation of dolomite. *Sedimentology*, **55**, 729–750.

Sanz-Montero, M.E., **Rodríguez-Aranda, J.P.** and **García del Cura, M.Á.** (2009) Bioinduced precipitation of barite and celestite in dolomite microbialites examples from Miocene lacustrine sequences in the Madrid and Duero basins, Spain. *Sediment. Geol.*, **222**, 138–148.

Segovia-Campos, I., **Martignier, A.**, **Filella, M.**, **Jaquet, J.M.** and **Ariztegui, D.** (2021) Micropearls and other intracelullar inclusions of amorphous calcium carbonate: an unsuspected biomineralization capacity shared by diverse microorganisms. *Environ. Microbiol.*, **24**, 537–550.

Stevenson, R.J. (1996) An introduction to algal ecology in freshwater benthic habitats. In: *Algal Ecology Freshwater Ecosystems* (Eds Stevenson, R.J., Bothwell, M.L. and Lowe, R.L.), pp. 3–26. Academic Press, New York, NY.

Toyokawa, C., **Yamano, T.** and **Fukuzawa, H.** (2020) Pyrenoid starch sheath is required for LCIB localization and the CO_2-concentrating mechanism in green algae. *Plant Physiol.*, **182**, 1883–1893.

Tucker, M.E. and **Wright, V.P.** (1990) *Carbonate Sedimentology*, p. 482. Blackwell Scientific Publications, Oxford.

Vasconcelos, C., **McKenzie, J.A.**, **Bernasconi, S.**, **Crujic, D.** and **Tiens, A.J.** (1995) Microbial mediation as a possible mechanism for natural dolomite formation at low temperatures. *Nature*, **377**, 220–222.

Wang, L., **Yamano, T.**, **Takane, S.**, **Niikawa, Y.**, **Toyokawa, C.**, **Ozawa, S.**, **Tokutsu, R.**, **Takahasi, Y.**, **Minagawa, J.**, **Kanesaki, Y.**, **Yoshikawa, H.** and **Fukuzawa, H.** (2003) Chloroplast-mediated regulation of CO_2-concentrating mechanism by Ca^{2+} binding protein CAS in the green alga *Chlamydomonas reinhardtii*. *Proc. Nat. Acad. Scie. USA*, **113**, 12586–12591.

Weiner, S. and **Dove, P.M.** (2003) An overview of biomineralization and the problem of the vital effect. In: *Biomineralization* (Eds Dove, P.M., Winer, S. and De Yoreo, J.J.), pp. 1–31. Mineralogical Society of America. Reviews in Mineralogy and Geochemistry, Washington, DC.

Xu, J., **Yan, C.**, **Zhang, F.**, **Konishi, H.**, **Xu, H.** and **Teng, H.** (2013) Testing the cation-hydration effect on the crystallization of Ca-Mg-CO_3 systems. *Proc. Nat. Acad. Scie. USA.*, **110**, 17750–17755.

Manuscript received 22 March 2022; revision accepted 27 September 2022

Supporting Information

Additional information may be found in the online version of this article:

Fig. S1. X-ray powder diffraction patterns of two suspended mats.

Fig. S2. Powder XRD diffractogram of non-dialyzed EPS collected in April 2018.

Fig. S3. Energy dispersive X-ray (EDX) spectra of point analyses carried out in the studied samples.

Table S1. Elemental composition in weight % of high magnesian calcite (HMC) and dolomite from fixed cells of *Spirogyra* varians determined by EDX analyses.